Full Text View

Volume 29, Issue 6 (June 1999)

Journal of Physical Oceanography
Article: pp. 1208–1220 | Abstract | PDF (222K)

Rotating Convection Driven by Differential Bottom Heating*

Young-Gyu Park

MIT/WHOI Joint Program in Oceanography, Woods Hole Oceanographic Institution, Woods Hole, Massachusetts

J. A. Whitehead

Department of Physical Oceanography, Woods Hole Oceanographic Institution, Woods Hole, Massachusetts

(Manuscript received January 14, 1998, in final form June 19, 1998)

DOI: 10.1175/1520-0485(1999)029<1208:RCDBDB>2.0.CO;2

ABSTRACT

Convection experiments were carried out in a rectangular tank as a model of oceanic meridional overturning circulation. The objective was finding a relation between the meridional heat flux and thermal forcing. To make the meridional heat flux estimate possible, the heat flux was fixed at one bottom end of the tank using an electrical heater. Temperature was fixed at the other end using a cooling plate. All other boundaries were insulated. In equilibrium, the heat input to the fluid H was the same as the meridional heat flux (heat flux from the source to the sink), so it was possible to find a scaling law relating H to the temperature difference across the tank ΔT and rotation rate f. The experimental result suggests that the meridional heat transport in the experiment was mostly due to geostrophic flows with a minor correction caused by bottom friction. When the typical values of the North Atlantic are introduced, the geostrophic scaling law predicts meridional heat flux comparable to that estimated in the North Atlantic when the vertical eddy diffusivity of heat is about 1 $cm^2\ s^{-1}$.

1. Introduction

The local imbalance between solar radiation and the earth's back radiation generates a meridional sea surface temperature gradient that drives a well-known vertical convective oceanic circulation. The circulation carries about half of the heat accumulated in the equatorial regions toward the polar regions (Vonder Haar and Oort 1973). Direct estimates using hydrographic data (Bryden and Hall 1980; Hall and Bryden 1982) also show that convective overturning circulation is important in meridional heat transport in the North Atlantic. The heat transport compensates the imbalance between solar radiation and

the earth's back radiation, and thereby reduces the temperature contrast between equatorial and polar regions. Therefore, such circulation is believed to be important in regulating the climate of the earth.

Rossby (1965) derived a functional relation for meridional overturning circulation in terms of buoyancy forcing, the vertical diffusivity of heat, and the viscosity. He confirmed the relation using his laboratory experiments, but his study lacked the effect of rotation. Bryan and Cox (1967) derived a scaling law for meridional heat transport based on geostrophy and advective–diffusive heat balance based on the classical thermocline theory by Robinson and Stommel (1959). Their numerical experiment and the ones by Bryan (1987), Colin de Verdière (1988), and Winton (1996) suggest that the relation is valid. In those studies, the main objective was to find the dependence of the overturning circulation on the exponent of vertical heat diffusivity κ. An overturning circulation of a salty ocean driven by freshwater flux at the surface also has been shown to follow the scaling law based on geostrophy and advective–diffusive salt balance (Huang and Chou 1994).

A laboratory experiment performed within a rotating rectangular container by Condie and Griffiths (1989) shows flows that carry heat from the source to the sink of heat. The temperature field of the experiment, however, was quite different from that of the oceans so that the experimental results may not be as applicable to the convective overturning circulation of the oceans as the present experiments. In the oceans, the buoyancy forcing is applied along the sea surface. In contrast, the thermal forcing of the experiment was applied through the opposing side walls. A horizontal thermal boundary layer, which is equivalent to the thermocline of the oceans, was not observed. An interior of uniform temperature was therefore not observed, either.

In the experiment by Speer and Whitehead (1988), thermal forcing was applied along the bottom of their rectangular tank. The experiment was primarily intended for oceanic application but the results were only qualitative and descriptive. The functional dependence of the structure of the flow and temperature field on external parameters was not found. Heat flux measurements were not made either.

In this study, an experiment on rotating convection driven by differential bottom heating has been performed. The experiment is intended to be governed by the basic physics of rotating convection in a rectangular tank and hence the thermal component of the thermohaline circulation. Given a surface heat flux distribution, we seek to answer the following main questions:

1. What are the scaling laws governing the temperature field and heat transport?
2. What does the convective flow field look like?
3. What are the strengths and limitations of this experiment as a model of oceanic overturning circulation?

In section 2, the scaling law based on geostrophy and advective–diffusive heat balance is reviewed. In section 3, the experimental design and procedures are discussed. In section 4, the experimental results are discussed while focusing upon the questions raised above. A brief summary and conclusion are drawn at the end.

2. The scaling law

The scaling law described in this section is based on the classical thermocline theory by Robinson and Stommel (1959) as in Bryan and Cox (1967) and subsequent studies (Welander 1971, 1986; Bryan 1987; Colin de Verdiére 1988; Whitehead 1991; Huang and Chou 1994;Winton 1996). Our formulation and wording differ from the above only in minor ways, but we review the assumptions used during the derivation of the scaling law carefully. Assume that a meridional (north–south) temperature difference ΔT is applied to the surface of water in a rectangular basin. The water near the cold (northern) end becomes dense and sinks rapidly to the bottom. The water then flows toward the hot (southern) end while ascending toward the surface. At the surface, water flows from the hot end toward the cold end within a thermal boundary layer, which is equivalent to the thermocline of the oceans.

Within the thermal boundary layer, the thermal wind balance yields a horizontal velocity scale U:

$$U \equiv \frac{g\alpha\Delta T\delta_T}{fl_y}, \qquad (1)$$

where g is gravitational acceleration, α is thermal expansion coefficient, δ_T is a scale of thermal boundary layer thickness, f is the Coriolis parameter, and l_y is the length of a basin. The above relation is for a zonal velocity scale. In a numerical study by Hughes and Weaver (1994), within the thermal boundary layer, the North Atlantic overturning is almost linearly proportional to the meridional difference in the zonal average of depth-integrated steric height between the latitude of

maximum zonally averaged surface density and the southern limit of the North Atlantic (1.75°N). The results suggests that the zonal temperature gradient (T_x) that drives the meridional overturning circulation is linearly proportional to the meridional temperature gradient (T_y). Therefore we can assume $T_x \sim T_y$ within the thermal boundary layer and meridional velocity scale $V = U$.

The meridional movement of a fluid must be compensated by upwelling into the thermal boundary layer, so a vertical velocity scale W results:

$$W \equiv \frac{V\delta_T}{l_y}. \qquad (2)$$

The balance between the downward diffusion of heat from the surface and vertical advection of the cold water at the base of the thermal boundary layer (Munk 1966),

$$wT_z \approx \kappa T_{zz},$$

yields

$$W \equiv \frac{\kappa}{\delta_T}. \qquad (3)$$

Here, κ is the thermal diffusivity. Horizontal diffusion of heat $\kappa(T_{xx}, T_{yy}) \sim \kappa\Delta T(l^{-2}{}_x, l^{-2}{}_y) \ll \kappa\Delta T\, \delta^{-2}{}_T \sim \kappa T_{zz}$ and is negligible in the heat equation. Here l_x is the width of the container. Horizontal advection of heat was not considered in the above relation but, if we use continuity,

$$\upsilon T_y \approx V\Delta T/l_y \approx W\Delta T/\delta_T \approx wT_z.$$

Thus, horizontal advection is as important as vertical advection.

Using the above three relations, one can get

$$\delta_T = \left(\frac{\kappa l_y^2 f}{g\alpha\Delta T}\right)^{1/3}, \qquad (4)$$

$$V = \left(\frac{\kappa(g\alpha\Delta T)^2}{l_y f^2}\right)^{1/3}. \qquad (5)$$

Meridional mass transport per unit width Q is then

$$Q = V\delta_T = \left(\frac{\kappa^2 l_y g\alpha\Delta T}{f}\right)^{1/3}. \qquad (6)$$

Meridional heat flux per unit width H/l_x is thus

$$\frac{H}{l_x} \equiv \rho_o C_p \Delta T Q$$

$$= \rho_o C_p \left(\frac{l_x g\alpha\kappa^2\Delta T^4}{f}\right)^{1/3}. \qquad (7)$$

Since a heat flux boundary condition was used in the experiment, it is more convenient to express ΔT and δ_T in terms of

H and other experimental parameters as follows:

$$\Delta T_{GS}(H, f) = \left(\frac{fH^3}{(l_x \rho_o C_p)^3 l_y g \alpha \kappa^2} \right)^{1/4}, \quad (8)$$

$$\delta_{T_{GS}}(H, f) = \left(\frac{\rho_o C_p l_x l_y^3 \kappa^2 f}{g \alpha H} \right)^{1/4}. \quad (9)$$

The scaling law is based on geostrophy (hence the subscript GS) and advective–diffusive heat balance, so it will be called a *geostrophic scaling law* hereafter.

A thermal boundary layer thickness is an indicator of heat transfer efficiency, independent of processes responsible for meridional heat transport. In equilibrium, heat loss by the system by deep-water mass formation H (heat input for an upside down ocean like the present experiment) is the same as meridional heat transport and diffusive heat input (loss) through the surface (bottom) excluding the water mass formation region. Therefore, $H \sim \kappa \Delta T/\delta_T$ and $\delta_T \sim \kappa \Delta T/H$. Here ΔT can be treated as buoyancy forcing and H meridional heat flux. When buoyancy forcing ΔT is fixed, a system with higher heat transfer efficiency gives higher H and subsequently a thinner thermal boundary layer. When H is fixed, ΔT and δ_T are the smallest in the most effective system.

3. The experiment

a. Design

The design of the present experiment is sketched in Fig. 1. The first priority of the experiment was to simulate the effect of the meridional boundaries of the oceans. To accomplish this a 100 cm × 100 cm × 20 cm rectangular tank was used. The second priority was to get a thermal boundary layer that is equivalent to the thermocline of the oceans. To meet this end differential heating was applied along the bottom for technical convenience. The experiment was equivalent to an upside-down f-plane ocean. We call the "meridional" direction of the experiment (y) the direction of the applied temperature gradient. The zonal direction of the experiment (x) is then perpendicular to the meridional direction and the direction of gravity.

The third priority was to optimize the precision of the heat flux estimate. In earlier laboratory experiments, differential heating was implemented by specifying temperature distribution along or across boundaries. Since it is difficult to measure temperature profiles right next to boundaries, heat input to the fluid could not be estimated easily. This prevented most of the earlier experiments from getting quantitative results related to heat flux. In this experiment, heat flux was fixed along the bottom using an electrical heater and a cooling plate while insulating all other boundaries.

An electrical heater of 100 cm × 20.3 cm connected to a constant voltage source was placed at one bottom end of the tank. The cooling plate was a copper plate of 100 cm × 20.3 cm and located at the other end. The plate was cooled by running water from a constant temperature water bath through copper tubing that was soldered below the plate. A Plexiglas plate of 100 cm × 59.4 cm, 1.3 cm thick, was placed between the heating pad and the cooling plate to prevent any heat exchange. The four walls of the tank were made of Plexiglas, 1.3 cm thick, to retard heat transfer. The outside of the tank was insulated further with Styrofoam, 5 cm thick.

If this system was left alone long enough to reach an equilibrium state and if all the boundaries were insulated perfectly, the same amount of heat applied by the heater H would be removed by the cooling plate. Therefore, the meridional heat flux from the heating pad to the cooling plate was the same as H. Special tests showed that the experiment reached the equilibrium state (Park 1996).

In the experiment, however, the insulation was not perfect so that the boundary heat flux and the actual meridional heat transport could be different. Hereafter, H_N or nominal heat flux means the boundary heat flux due to the heating pad, and H means the actual (or corrected) meridional heat flux after the correction due to the imperfect insulation, which is described in detail in appendix A.

b. Parameters

The main nondimensional parameters of the experiment were

$$\text{Rayleigh number:} \qquad \mathrm{Ra} = \frac{g\alpha\Delta T l_y^3}{\nu\kappa}$$

$$\text{Ekman number:} \qquad E = \frac{\nu}{f d^2}.$$

Here, v is the kinematic viscosity of water, and d = 12 cm is the water depth. In the experiment, $5 \times 10^{10} < \mathrm{Ra} < 3.3 \times 10^{11}$ and $5.4 \times 10^{-5} < E < 2.7 \times 10^{-4}$, as listed in appendix B along with other experimental parameters. In turbulent ocean, $v \approx \kappa \approx 1 \times 10^{-4}$ m^2 s^{-1}, and Ra $\approx 10^{25}$. Therefore, we wanted to obtain large Ra in the experiment and a tank larger than those in similar experiments is used.

There are two other parameters related to Ra and E, which more clearly indicate the importance of rotation or balance in a thermal boundary layer (Hignett et al. 1981). One is a thermal boundary layer thickness that is small when buoyancy forcing is strong. For this, one can use the thermal boundary layer thickness of a nonrotating system $\delta_{T_n} = l_y \mathrm{Ra}^{-1/5}$ (Rossby 1965), where the subscript n stands for nonrotating system and l_y is the length of the tank. The other, which is small when rotation is strong, is the Ekman layer thickness in a homogeneous fluid $\delta_E = dE^{1/2}$. The square of the ratio between the two thickness scales,

$$r \equiv \left(\frac{\delta_T}{\delta_E}\right)^2 = \mathrm{Ra}^{-2/5} E^{-1} \left(\frac{l_y}{d}\right)^2 \sim f \Delta T^{-2/5}, \qquad (10)$$

stands for the importance of rotation in convection (Hignett et al. 1981).

When $r > O(1)$, a thermal boundary layer is thicker than the Ekman layer; rotation is important. When $r < O(1)$, the Ekman layer is thicker than a thermal boundary layer; frictional dissipation is important within the thermal boundary layer. In the oceans, the Ekman layer is O(100 m) deep (using an empirical turbulent viscosity), but the thermocline is about 1000 m. The thermal boundary layer of the experiment should be thicker than the Ekman layer so that geostrophy is maintained within the thermal boundary layer. Both Ra and E were varied independently to get $r > O(1)$ and most of the runs were done with this range.

c. Procedure

The longest timescale of the experiment is diffusive timescale $T_d \approx d^2/\kappa \approx 28$ h. To satisfy the flux boundary condition a run should reach an equilibrium state so that the water was spun up at least 40 h before temperature sections were made. Temperature measurement during the spinup shows that the experiment reached an equilibrium state after about 35 hours of spin up (Park 1996).

Temperature sections were made after the hourly average of the readings with the two thermistors changed less than 0.1° C. Temperature was measured with a rack mounted array of thermistors at 7 to 13 levels with at least 15 locations on each level at each section. The uncertainty in temperature measurement due to the accuracy of the thermistors, ±0.1°C, was small compared to the error in heat loss due to imperfect insulation and neglected.

Three meridional sections were taken in most runs: 10 cm away from the left and right meridional boundaries and one at the center (x = 10 cm, 50 cm, 90 cm). The horizontal position was determined manually so its uncertainty was ±5 mm or less. Zonal sections were made for selected parameters at selected locations to identify heat carrying flows and to infer flow patterns. It took about two to three hours to complete a section. To remove disturbances that might have occurred during the measurement, the experiment was left at least four hours before making another section. Including the spinup time, a run took about three to four days.

Flow visualization was done using the thymol blue technique. A stack of two grids was used as electrodes. Each grid consisted of one or more meridional and three or more zonal wires of 0.16-mm diameter stainless steel rods. One grid was placed 1 cm above the bottom, so it was within the thermal boundary layer but above the Ekman layer. The other one was placed 7 cm above the bottom to be in an interior of homogeneous temperature.

4. Results

a. Temperature distribution

1) MERIDIONAL SECTIONS

The meridional temperature distribution (Fig. 2) is qualitatively similar to that of Rossby (1965) (Fig. 5b in the paper) and Speer and Whitehead (1988) (Fig. 5 in the paper). A thin thermal boundary layer extended from the cold end toward the hot end along the bottom of the tank. A rising region, where stratification was zero, or close to zero, was confined to a small region near the hot end. The interior temperature was uniform and close to that of the rising region.

When Figs. 2a and 2b are compared, the interior temperature increases as f increases, although H_N is fixed. As f increases, vertical motion becomes more difficult and convective circulation becomes weaker. The water over the heating pad was exposed to the heat from the heating pad more before it filled the interior so that the interior temperature became higher. A run with higher H_N shows obviously higher interior temperature, as the comparison between Figs. 2b and 2c shows.

From the meridional temperature sections the temperature difference ΔT between the heating pad and the cooling plate (T_B) was estimated. Sometimes the hottest temperature was measured not at the bottom but in the interior. Temperature was measured at discrete locations, so it was possible to miss the hottest point. The temperature difference between the hottest water observed in the interior and the water near the heating pad was small, however. Since there was no other source of the heat than the heating pad, the highest temperature measured $T_{\max}$, irrespective of the location, was considered the temperature of the heating pad. The estimated temperature change across the cooling plate made of 0.32 mm thick copper plate was less than the accuracy of the thermistors (0.1°C). The temperature of the cold water bath was effectively the same as T_B, so

$$\Delta T = T_{\max} - T_B.$$

2) VERTICAL PROFILES

In Fig. 3 three normalized vertical temperature profiles at $(x, y) = (49.5\text{ cm}, 96\text{ cm})$ are shown using the center of the probes for the depth of the measurement. A solid line is the least squares fit of a temperature profile to an exponential function, $1 - e^{-z/a_1}$, where z is height and a_1 is a constant that minimizes the residual between the fit and the data. The constant a_1 for each case is comparable to the scale of the thermal boundary layer thickness, whose details are described in section 4d. In the thermal boundary layer less than 2 cm thick, temperature changed very rapidly so that it was not possible to resolve it with 2-mm diameter thermistors, especially right near the bottom. Measurements, however, were adequate for the estimation of a thermal boundary layer thickness as shown in section 4d. When the vertical temperature gradient is small, one can get a better temperature profile so that the fit becomes better as h increases.

b. Flow pattern

A schematic flow pattern compiled from the flow visualization made in various locations is presented in Fig. 4. The flows within the thermal boundary layer and over the cooling region as shown in Fig. 5 are of interest. The visualization method is equivalent to placing a source of neutrally buoyant dye at a fixed location so that the figure represents streak lines. Over the heating region active mixing induced by vertical convection made it hard to get clear flow patterns.

The dye streak shows that there is a cold current toward the cold end along the wall to the left near the upper left corner (flow I). The flow becomes zonal when it meets the cold end wall and flows anticyclonically along the cold end wall. When the flow reaches the meridional wall to the right, it turns toward the hot end wall (flow II). Near the end of the cooling plate, most of the cold water turns toward the wall to the left and becomes zonal. The remaining part of the cold water continues to flow toward the hot end along the wall to the right. As the zonal flow approaches the wall to the left, most of it turns toward the hot end (flow III) and brings cold water to the hot end along the wall to the left (flow IV); the remaining part of the cold water joins to flow I and returns to the cold end, completing an anticyclonic circulation as sketched in Fig. 4.

The zonal temperature section (Fig. 6a) shows two cold water masses at both ends, consistent with the flow pattern. Over the cooling plate, the water cools while it circulates so there is more cold water near the wall to the right. The cold water turns to the left near the edge of the cooling plate and the major cold flow from the cold end toward the hot end is along the wall to the left (flow IV) so that the center zonal section (Fig. 6b) shows more cold water near the wall to the left. There is another cold flow (flow V) near the wall to the right, but it is weak compared to flow IV.

Warm water starts near the lower-left corner and flows toward the upper-right corner (flow VII). It extends almost to the bottom so that the flow toward the cold end in Fig. 5b (flow VII-B) is not cold water but warm water as can be seen in the zonal temperature section Fig. 6b. When the warm water (flow VII) reaches near the cooling plates, it splits into two, as sketched in Fig. 4. The water closer to the cold end turned cyclonically due to vortex column stretching and becomes flow VI. This cyclonic motion is similar to that in the experiment of Speer and Whitehead (1988) in which the flow pattern of the homogeneous interior is described mostly. The water closer to the hot end turned anticyclonically along the edge of the thermal boundary layer to conserve its potential vorticity and becomes flow VIII.

Between the center meridional section and the section near the cooling plate, the cold flow is mostly zonal. Until the warm water reaches the cooling plate, the water could maintain its heat content and the meridional temperature gradient along the bottom remains small. As the water flows over the cooling plate, the cooling starts and the thermal boundary layer is formed. The meridional temperature gradient that supported the zonal flow becomes larger over the boundary between the cooling plate and the insulating center plate (60 cm < y < 90 cm in Fig. 2). The temperature gradient makes the boundary condition of this experiment different from those of numerical models or experiments, which were sinusoidal or linear. The temperature and velocity distribution of this experiment, especially near the boundary between the cooling plate and the middle plate, might be different from those of other studies. However, we are more interested in scaling laws related to large-scale features and the experiment met this purpose.

The flow pattern is more complicated than those in numerical experiments on convective circulation in f planes (Colin de Verdière 1988; Winton 1996). The circulation over the cooling plate, however, is similar to those. To compensate for the diffusive heat loss through the cooling plates, warm water sinks into the thermal boundary layer. The warm water experiences vortex column stretching, and a cyclonic circulation is induced. The cold water experiences vortex column compression and an anticyclonic circulation is induced as sketched in Fig. 4.

In addition to the mean circulation, the visualization shows that there are many eddies in the warm water, whereas there are fewer in the cold water. The eddies within the warm water could not contribute heat transport because meridional temperature gradient in the warm water was almost zero. The eddies near the boundary between the cold water and warm water were expected to enhance mixing and heat transport locally.

The heat loss through the walls of the tank could deform isotherms and induce flows. The water in the tank was always warmer than room temperature. The heat loss was from the water to the environment so that the temperature should decrease toward the walls. The stratification was stable except in the water-mass formation region, so $\partial T/\partial z > 0$. Therefore, isotherms must tilt upward toward the wall within the diffusive layer. If diffusion is a dominant process near the walls, isotherm tilt near walls should be universal in temperature sections. Such isotherm tilt can be found in some locations (in Figs. 6b,c, near x = 100 cm), but there is no reason for the heat loss to be confined to those locations; the tilt is not related to the diffusive layer but to the interior geostrophic flows. In Figs. 6b and 6c, 0.9 isotherms near x = 0 cm are vertical. They might be due to convective motion from the side wall heat loss. The thickness of the side wall boundary layer is then about 3 cm. The flow visualization, however, does not show any significant difference in flow pattern within about 3 cm from the walls; the heat loss through the side wall did not seem to modify the flow noticeably.

During the visualization, when the cover was removed, the formation of eddies a few centimeter-wide, which were significantly smaller than those in Fig. 5, occurred throughout the tank within a few minutes. The eddies were due to the heat loss through the surface of the water. The evaporative heat loss also could generate such eddies. The surface water temperature was uniform so that the formation of the eddies, which could modify the heat transport efficiency, could not be localized. In any case, the evaporative heat loss and the effect of the eddies are included in the uncertainty of H as described in appendix A.

c. A test of scaling laws

1) MERIDIONAL HEAT TRANSPORT

In Fig. 7, f versus ΔT for H_N = 50 W is shown along with the scaling law. Although H_N was fixed, H varied depending on f. The least squares fit using the experimental results from the runs with the same f shows that $\Delta T \sim H^{0.61}$. Note that the exponent 0.61 is smaller than that predicted by the scaling law ¾. In Condie and Griffiths (1989), the ratio of the heat transport by convection to conduction, the Nusselt number Nu $\sim$ Ra$^{1/4}$. Therefore, $H/\Delta T \sim \Delta T^{1/4}$ and we get $H \sim \Delta T^{5/4}$. If we invert the relation we get $\Delta T \sim H^{4/5}$. Their power relation is significantly different from that of the present experiment. The experimental power relation is used to extrapolate experimental results to constant heat flux. If the above correction is neglected, the power law dependence decreases by about 10%. The slope of the least squares fit line is 0.13 so it is significantly smaller than that of the scaling law ¼. In Condie and Griffiths (1989) Nu $\sim f^{-0.05}$ and Nu $\sim \Delta T^{1/4}$. Therefore, we get $\Delta T \sim f^{-0.2}$, which is quite different from the present experimental result. The difference between their

experimental configuration and the present one, as explained in the introduction, is the most likely cause of the difference.

2) THERMAL BOUNDARY LAYER THICKNESS

The thickness of a thermal boundary layer, δ_T, was estimated using temperature profiles at (x, y) = (49.5 cm, 96 cm) such as Fig. 3. The top of each boundary layer was defined as the depth at which $T_n = 0.9$. The resolution of the profile was not high enough to obtain accurate estimate of the e-folding scale ($T_n = 0.63$). When $T_n > 0.9$, the temperature gradient was so small that uncertainty in temperature can cause large error in the estimation. The results with $T_n = 0.8$ (not shown here) are similar to those with $T_n = 0.9$. The thickness was measured with a ruler from the profiles with 5-mm resolution at best, thus a typical error was about ±2.5 mm. As H was increased, the thermal boundary layer became thinner. The resolution became poorer and the error increased.

The results for $H_N = 50$ W in an (f, δ_T) space are shown along with the scaling laws in Fig. 8. In Table 1, the power dependence of δ_T on f using the linear least squares fit is presented for four fixed values on H_N. In the runs with $H_N > 200$ W, the thermal boundary layers were so thin that useful results could not be obtained, and they were excluded. The mean power dependence of δ_T on f is 0.32 and becomes close to that of the geostrophic scaling law if the results with $H_N = 200$ W, in which $\delta_T < 2$ cm so that the error was large, are excluded.

d. A corrected scaling law

The comparisons in the previous section show that the power dependence of δ_T on f follows the scaling law but the meridional temperature difference does not. The scaling law does not allow any frictional effects, but in the experiment there was always a frictional Ekman layer at the bottom. A correction to the geostrophic scaling law due to the bottom Ekman layer can be made since the thermal boundary layer of the experiment was thicker than the Ekman layer.

First, within the Ekman layer, the friction reduced the meridional velocity as sketched in Fig. 9. The meridional mass transport, and consequently heat transport, were weakened. Second, there might be temperature change across the Ekman layer since the Ekman layer is within the thermal boundary layer. (In Hignett et al. 1981, this temperature change was ignored.) The meridional temperature gradient at the top of the Ekman layer that forced the interior geostrophic flow would be weaker than that along the bottom. The reduced heat transport efficiency would then require a thicker thermal boundary layer or higher thermal forcing to maintain the same amount of meridional heat transport. As f weakened, the Ekman layer thickened so that the effects became larger; the power dependence of ΔT on f would decrease. For fixed f, as H increases, δ_T becomes thinner and the Ekman layer becomes relatively thicker. Therefore, the bottom friction also weakened the power dependence of ΔT on H as the experimental results shows in section 4c.

The geostrophic flow away from the Ekman layer is assumed to be driven by T_G,

$$\Delta T_G = \Delta T_C - \Delta T_F,$$

where, as sketched in Fig. 9, ΔT_F is the temperature drop across the Ekman layer and ΔT_C is a "corrected" temperature change (which we picture as equal to ΔT that we measured). The temperature profile is exponential (Fig. 3), so

$$T = T_I - (T_I - T_B)\exp(-z/\delta_{T_C}).$$

Here T_I is interior temperature, T_B is the temperature of the cooling plate (therefore $\Delta T = T_I - T_B$), and δ_{T_C} is a corrected thermal boundary layer thickness. From the above temperature distribution, we can define

$$\Delta T_F = T_I - T(\delta_E)$$

and

$$\Delta T_G = \Delta T \exp(-\delta_E/\delta_{T_C}).$$

Here, the Ekman layer thickness $\delta_E = (2\nu/f)^{1/2}$.

In region I, geostrophy is valid so the thermal wind relation yields a velocity scale,

$$V_G \sim \frac{g\alpha\Delta T_G(\delta_{T_C} - \delta_E)}{f l_y},$$

since the thickness of region I is $(\delta_{T_C} - \delta_E)$. In region II, the Ekman flux is driven by a geostrophic flow of V_G in a homogeneous fluid (Pedlosky 1987), which is the same as the retarding Ekman flux

$$Q_E = V_G\delta_E/2.$$

The total meridional mass flux Q is

$$Q = Q_G + Q_E \sim U_G(\delta_{T_C} - \delta_E) + U_G\delta_E/2.$$

From the heat equation $wT_z \approx \kappa T_{zz}$,

$$\delta_{T_C} \sim \frac{\kappa}{W} \sim \frac{\kappa l_y}{Q};$$

here the continuity $W \sim Q/l_y$ has been used. Meridional heat flux per unit width H/l_x is then

$$\frac{H}{l_x} \sim \rho_o C_p[U_G\Delta T_G(\delta_{T_C} - \delta_E) + U_G\Delta T_C\delta_E/2].$$

The first term within brackets is due to the geostrophic meridional flow in region I, where the meridional temperature difference is ΔT_G. The second term is due to the sum of the interior geostrophic flow and the retarding Ekman transport in region II, where the meridional temperature difference is ΔT_C.

If we assume $\delta_E/\delta_{T_C} < O(1)$, we can expand all the variables using δ_E/δ_{T_C}. Since the thermal boundary layer thickness for a nonrotating system $\delta_{T_n} < \delta_{T_C}$ and $r^{-1/2} = \delta_E/\delta_{T_n}$, $\delta_E/\delta_{T_C} < r^{-1/2}$. The condition $r > O(1)$, in which we are interested and most of the runs satisfy, makes the error of the expansion $(\delta_E/\delta_{T_C})^2 = r^{-1} < O(1)$. If we expand the variables using δ_E/δ_{T_C} and solve with respect to external parameters H and f,

$$\Delta T_C \sim (\rho_o C_p g\alpha)^{1/2}(fH)^{1/2}\left(1 - \frac{7}{2}\frac{\delta_E}{\delta_{T_C}}\right)^{-1/2}\delta_{T_C}^{-1} \quad (11)$$

and

$$\delta_{T_C} \sim \frac{3}{4}\delta_E + \left[\frac{9}{16}\delta_E^2 + \left(\frac{l_x l_y^3\kappa^2\rho_o C_p}{g\alpha}\right)^{1/2}\left(\frac{f}{H}\right)^{1/2}\right]^{1/2}. \quad (12)$$

The above relations can be written using the ones from the geostrophic scaling law ΔT_{GS} [Eq. (8)] and $\delta_{T_{GS}}$ [Eq. (9)] as follows:

$$\delta_{T_C} \sim \delta_{T_{GS}} \left(1 + \frac{3}{4}\frac{\delta_E}{\delta_{T_{GS}}}\right). \qquad (14)$$

As expected, the correction becomes larger as f becomes slower so that δ_E becomes larger. By introducing the main external parameters, H and f, to Eq. (12), one can calculate δ_{T_C}, which in turn can be used to obtain ΔT_C using Eq. (11).

The relation between f and ΔT_C from the corrected scaling law when H_N = 50 W is shown in Fig. 7 as a thick solid curve. Since the corrected scaling law is a polynomial, we cannot obtain a unique power law but we can obtain an average value. The correction weakens the power dependence of ΔT_C on f from 0.25 to about 0.17, which is closer to the experimental result 0.12. The relation between δ_{T_C} and f from the corrected scaling law when H_N = 50 W is shown in Fig. 8 as a thick solid line. The correction weakens the power dependence, but the change is small compared to the scatter in the experimental data.

In Fig. 10, ΔT from the experiment and the corrected scaling law ΔT_C using Eq. (13) are compared. In the figures, the runs with $r > O(1)$ were used. The uncertainty in ΔT_C, which arises principally from the 20% uncertainty in H, is about 10%. The variations in the temperature measurement cause about 3% uncertainty in $\Delta T_{\rm exp}$. It is small compared to the error in H, and neglected. The thermal expansion coefficient α increases with temperature so it is assumed a linear function of temperature. The effect, however, is small compared to the uncertainty in ΔT_C.

We found the following relation from the linear least squares fit:

$$\Delta T_{\rm exp} = 10^{0.61\pm0.02}\ \Delta T_C^{0.79\pm0.04}. \qquad (15)$$

If all the meridional heat transport could be explained by the scaling law, $\Delta T_{\rm exp}$ and ΔT_C should show a linear relation, that is, $\Delta T_{\rm exp} \sim \Delta T_C^1$ as the dashed line in the figure, within the uncertainty interval of the experiment. Although such a linear relation is outside of the experimental fit [Eq. (15)], the fit itself is good since the uncertainty interval is small and no point is away from the fit. The internal parameter ΔT is determined by two external parameters f and H_N, which were varied independently by a factor of 10. Unless the dependencies of ΔT on the external parameters are similar in the experiment and the scaling law, such a fit cannot be obtained. The differences between the experiment and the corrected scaling law are small, so the scaling law can be considered as a first approximation of the experiment.

The power dependence in Eq. (15) is less than 1, so the experimental result is less sensitive than the corrected scaling law. There are processes in the experiment that contribute to the meridional heat transport in addition to the geostrophic flows. The condition for baroclinic instability in the thermal boundary layer is (Pedlosky 1987)

$$\frac{N\delta_T}{f} < l_{\rm bc}\frac{2.399}{\pi},$$

where $N^2 = -g\alpha T_z$ and $l_{\rm bc}$ is the length scale of baroclinic region. In the experiment, $N\delta_T/f \approx 20$ cm and $l_{\rm bc}$ is comparable to the length of the tank; baroclinic eddies could develop. The flow visualization shows that there were many eddies in the experiment. Although baroclinic eddies are not efficient enough to explain all of the meridional heat transport in the experiment, they could contribute to the heat transport. The residual in the fit ($\Delta T_{\rm exp} - 10^{0.61}\Delta T_C$) is comparable to the heat transport estimated from a simple scaling law based on baroclinic eddies, such as Stone (1972), but a statistically significant relation between them could not be obtained.

If we assume a linear relation between $\Delta T_{\rm exp}$ and ΔT_C, we get

$$\Delta T_{\rm exp} = \Delta T_{G,\rm exp} + \Delta T_{F,\rm exp} \approx 2.2\Delta T_C = 2.2(\Delta T_G + \Delta T_F)$$

from the least squares fit. Thus,

$$\Delta T_{G,\mathrm{exp}} \approx 2.2\Delta T_G.$$

If we assume $\Delta T_{G,\mathrm{exp}}$ is fixed, and estimate meridional heat transport using the geostrophic scaling law, we get

$$H_{G,\mathrm{exp}} = C_1 h \Delta T^{4/3}_{G,\mathrm{exp}} = C_1 h (2.2\Delta T_G)^{4/3},$$

where C_1 is a proportionality constant of heat transport relation, and h is a function of the constants related to the physical properties of water and geometry of the tank. Since $h\Delta T^{3/4}_G = H_{G,\mathrm{exp}}$, we obtain

$$C_1 = 2.2^{-4/3} = 0.35.$$

In the Bryan and Cox (1967) numerical experiment, the proportionality constant for the meridional heat transport is about 0.3, comparable to the experimental result of 0.35. If a similar conversion is done with the proportionality constant in Eq. (15), $10^{0.6}$, we get 0.16. The proportionality constant for meridional transport must be within 0.26 ± 0.1.

The correction due to the bottom friction was also applied to thermal boundary layer thickness. In Fig. 11, the corrected scaling law [δ_{T_C} from Eq. (14)] and the experimental results (δ_T) are compared. The uncertainty in δ_{T_C} is due to that in H, and the error in δ_T is from the resolution of vertical temperature profiles. The least squares fit to all data, the thin solid line in the figure, is

$$\delta_{T_{\mathrm{exp}}} = 10^{-0.18\pm0.05}\delta^{1.4\pm0.24}_{T_C}.$$

The relation is not linear but the deviation is mostly due to the runs with $\delta_T < 2$ cm so that the resolution of the profiles, which was 5 mm, was not high enough to give a reasonable estimation of δ_T. If the runs of $\delta_T < 2$ cm are excluded, the least squares fit to the data, the thick solid line in the figure, is

$$\delta_{T_{\mathrm{exp}}} = 10^{0.04\pm0.07}\delta^{0.94\pm0.35}_{T_C}. \quad (16)$$

Although the large errors in the data make the uncertainty interval of the fit large, the linear law is within the uncertainty interval. The values of δ_T are small and the scatter is large, so the correction of the frictional effect does not show much effect.

5. Summary and discussion

A convection experiment was performed as a model of the thermohaline circulation of the oceans. Buoyancy forcing was applied by differentially heating the bottom of a rectangular tank using an electrical heater of constant heat flux and a cooling plate of constant temperature. Therefore, the experiment was equivalent to an upside-down f-plane ocean with constant boundary heat flux. In equilibrium, the heat flux due to the heating pad was equivalent to the meridional heat flux within the experimental error. Since the meridional heat flux was a known experimental parameter, the temperature measurement with an array of thermistors allowed us to study a scaling law for the meridional heat flux for the first time in such a laboratory convection experiment. A scaling law for a thermal boundary layer was also studied.

A thin thermal boundary layer along with an interior of almost homogeneous temperature was observed, in agreement with other convection experiments with differential bottom heating. The comparison between the experiment and a scaling law developed earlier showed that most of the meridional heat flux was due to the meridional geostrophic flow with a minor correction for bottom friction. The same applied to the thermal boundary of the experiment.

Zonal temperature sections and flow visualization showed that over the cooling plate, the cold water circulated anticyclonically and the warm water above the cold water circulated cyclonically. The flow pattern over the cooling plate is consistent with a simple balance between the compression (in the cold water) or stretching (in the warm water) of a vortex column. Most of the cold water flowed toward the hot end along the wall to the left (looking from the hot end to the cold end). The hot flow toward the cold end was along the center of the tank but most of that water returned to the hot end along the side walls.

The experiment lacks the β effect, which is one of the important factors of real oceans. The thermocline thickness scale

δ_T from the classical thermocline theory by Robinson and Stommel (1959), on which the geostrophic scaling law is based,

$$\delta_T = \left(\frac{\kappa L f^2}{g \alpha \beta \Delta T} \right)^{1/3}, \qquad (17)$$

contains β explicitly. In planetary-scale motion $\beta \approx f/L$, where L is the size of a basin. If the relation is used in Eq. (17), the equation becomes the same as that from the geostrophic scaling law Eq. (4).

Winton (1996) performed a series of numerical experiment in which β was varied. When β was varied from zero to the standard value of the oceans 2×10^{-11} m^{-1} s^{-1} with $f_o = 10^{-4}$ s^{-1}, the meridional heat transport was increased by 20%. This does not necessarily prove that the β effect does not play any role in the meridional overturning circulation, but it tells us that f determines most of the meridional heat transport at least within the parameter range of oceanic relevance.

a. Application of the scaling law to the oceans

Naturally, this experiment is a very idealized model of the oceanic convective circulation, so we do not claim that the geostrophic scaling applies in detail to the oceans. The scaling law, however, contains the global effect of the thermohaline circulation, so it can be applicable to simple climate models. For example, Park (1999) incorporated the scaling law to Stommel's (1961) two-box model and found that the present thermohaline circulation of the North Atlantic is significantly more stable than those in models similar to Stommel's classical one.

The oceanic meridional heat transport is a global property so we compared that estimated using the geostrophic scaling law and that from observation. The estimation of the total meridional heat transport in the North Atlantic across 25°N using hydrographic data is 1.22×10^{15} W (Bryden and Hall 1980; Hall and Bryden 1982). If the contribution due to the surface Ekman flux driven by the wind 0.42×10^{15} W is excluded from the total, the estimation becomes 0.8×10^{15} W. If the canonical oceanic values related to the physical properties of the ocean, $l_x = 5000$ km, $l_y = 5000$ km, $d = 4$ km, $\kappa = 1$ cm^2 s^{-1}, and $\Delta T = 20$°C are substitute to the scaling laws $H = 1.3 \times 10^{15}$ W.

If the proportionality constant from the experiment, which is 0.26, is applied, the geostrophic scaling law predicts $H = 0.35 \times 10^{15}$ W. The value is half of the estimated heat flux in the North Atlantic. Considering that there are heat fluxes across the equator in the Atlantic and one due to the wind-driven gyres (and no equivalence in the experiment), which are included in that value of 0.8×10^{15} W, the prediction from the experiment is comparable to the estimation. The meridional heat transport of the North Pacific is also available (Bryden et al. 1991), but deep-water mass formation does not occur there (Warren 1983). It is not appropriate for comparison.

The estimations of the abyssal eddy diffusivity from microstructure measurement shows that κ varies spatially (Toole et al. 1994), although it is assumed uniform throughout this study. The estimated average value, furthermore, is 0.1 to 0.5 cm^2 s^{-1} and smaller than that used in the estimation of the North Atlantic meridional heat transport. The estimation of κ, however, becomes larger by up to 2 cm^2 s^{-1} near slopes in some regions. In the thermocline layer or the western boundary, the motion is more active so that turbulent and eddy diffusivity would increase. A reliable value of κ is not available yet, so we conclude only that, when $\kappa \approx 1$ cm^2 s^{-1} within the upper 1000 m of the oceans, the geostrophic scaling law predicts a meridional heat transport comparable to that observed in the North Atlantic.

The thermocline depth from the scaling law is about 200 m, so it is much smaller than the oceanic one. The thermocline depth is primarily determined by the surface wind-driven dynamics, while the thickness of the thermocline is determined by the vertical diffusivity of heat (Salmon 1990). Furthermore, there is no clear way of extracting the effect of the wind-driven circulation on the thermocline depth as yet, and the scaling law for convective overturning is not expected to provide a valid estimate of thermocline depth.

Acknowledgments

We thank to Drs. K. Helfrich, G. Flierl, R. X. Huang, J. Marotzke, and N. Hogg for their valuable comments and suggestions. We also thank the anonymous reviewers and Dr. K. Bryan for their suggestions. This study has been funded by NSF Grant OCE92-01464. Y.-G. Park also received partial support from Korean Government Overseas Scholarship Grant.

REFERENCES

Bryan, F., 1987: Parameter sensitivity of primitive equation ocean general circulation models. *J. Phys. Oceanogr.*, **17,** 970–985.. Find this article online

Bryan, K., and M. D. Cox, 1967: A numerical investigation of the oceanic general circulation. *Tellus,* **19,** 54–80..

Bryden, H. L., and M. M. Hall, 1980: Heat transport by currents across 25°N latitude in the Atlantic Ocean. *Science,* **207,** 884–886..

— ,D. H. Roemmich, and J. A. Church, 1991: Ocean heat transport across 24°N in the Pacific. *Deep-Sea Res.*, **38,** 297–324..

Colin de Verdière, A., 1988: Buoyancy driven planetary flows. *J. Mar. Res.*, **46,** 215–265..

Condie, S. A., and R. W. Griffiths, 1989: Convection in a rotating cavity: Modeling ocean circulation. *J. Fluid Mech.*, **207,** 453–474..

Hall, M. M., and H. L. Bryden, 1982: Direct estimates of ocean heat transport. *Deep-Sea Res.*, **29,** 339–359..

Hignett, P., A. Ibbetson, and P. D. Killworth, 1981: On rotating thermal convection driven by non-uniform heating from below. *J Fluid Mech.*, **109,** 161–187..

Huang, R. X., and R. L. Chou, 1994: Parameter sensitivity study of saline circulation. *Climate Dyn.*, **9,** 391–409..

Hughes, T. M., and A. J. Weaver, 1994: Multiple equilibria of an asymmetric two-basin ocean model. *J. Phys. Oceanogr.*, **24,** 619–637.. Find this article online

Munk, W. H., 1966: Abyssal recipes. *Deep-Sea Res.*, **13,** 707–730..

Park, Y.-G., 1996: Rotating convection driven by differential bottom heating. Ph.D thesis, MIT/WHOI, 140 pp..

— ,1999: Stability of the thermohaline circulation in a two-box model. *J. Phys. Oceanogr.*, in press..

Pedlosky, J., 1987: *Geophysical Fluid Dynamics.* 2d ed. Springer-Verlag, 710 pp..

Robinson, A., and H. Stommel, 1959: The oceanic thermocline and the associated thermohaline circulation. *Tellus,* **2,** 295–308..

Rossby, H. T., 1965: On thermal convection driven by non-uniform heating from below: an experimental study. *Deep-Sea Res.*, **12,** 9–16..

Salmon, R., 1990: The thermocline as an “internal boundary layer.” *J. Mar. Res.*, **48,** 437–467.

Speer, K. G., and J. A. Whitehead, 1988: A gyre in a non-uniformly heated rotating fluid. *Deep-Sea Res.*, **35,** 1069–1077..

Stommel, H. M., 1961: Thermohaline convection with two stable regimes of flow. *Tellus,* **13,** 224–230..

Stone, P. H., 1972: A simplified radiative–dynamical model for the static stability of rotating atmospheres. *J. Atmos. Sci.*, **29,** 405–418.. Find this article online

Toole, J. M., K. L. Polzin, and R. W. Schmitt, 1994: New estimates of diapycnal mixing in the abyssal ocean. *Science,* **264,** 1120–1123..

Vonder Haar, T. H., and A. H. Oort, 1973: New estimate of annual poleward energy transport by northern hemisphere oceans. *J. Phys. Oceanogr.*, **3,** 169–172.. Find this article online

Warren, B. A., 1983: Why is no deep water formed in the North Pacific? *J. Mar. Res.*, **41,** 327–347..

Welander, P., 1971: The thermocline problem. *Philos. Trans. Roy. Soc. London, Series A,* 415–421..

— ,1986: Thermocline effects in the ocean circulation and related simple model. *Large-Scale Transport Processes in Oceans and Atmosphere,* J. Willebrand and D. L. T. Anderson, Eds., Reidel, 163–200..

Whitehead, J. A., 1991: Small and mesoscale convection as observed in the laboratory. *Deep Convection and Deep Water Formation,* P. C. Chu and J. C. Gascard, Eds., Elsevier Science, 355–368..

Winton, M., 1996: The role of horizontal boundaries in parameter sensitivity and decadal-scale variability of coarse-resolution ocean general circulation models. *J. Phys. Oceanogr.*, **26,** 289–304.. Find this article online

APPENDIX A

6. Correction to the Meridional Heat Transport

The largest source of error is heat loss through the boundaries of the tank owing to imperfect insulation. The actual heat loss was estimated as follows. The tank was filled with hot water and left alone. Since no heating or cooling was applied, temperature change was solely due to the imperfect insulation. The heat loss was estimated by measuring the change of the water temperature. During the measurement, the water was mixed to make it homogeneous. The ratio of the heat loss to the temperature difference between the water and the laboratory was about 3 W °C^{-1}.

The conductive heat loss through the Styrofoam insulation was

$$(\rho_S C_{pS} \kappa_S / 5\ \text{cm}) \times \text{surface area of the tank} = 1.2\ \text{W}\ ^\circ\text{C}^{-1},$$

where the heat conduction coefficient of Styrofoam $\rho_S C_{pS} \kappa_S = 3 \times 10^{-4}$ J cm^{-1} s^{-1} °C^{-1}. To allow access to the water the cover of the tank was placed over the walls of the tank. The contact between the cover and the walls was not airtight, so warm air could escape from the tank to the laboratory in addition to the evaporation through the thermistor insertion slots. The remaining 1.8 W °C^{-1} must be due to the evaporative heat loss.

The heat loss was always from the water to the environment so that the upper bound of the meridional heat transport H_U:

$$H_U = H_{\text{heating pad}} = H_N.$$

The lower bound of the meridional heat transport H_L is

$$H_L = H_U - (T_{\text{water}} - T_{\text{lab}}) \times 3.0\ \text{W}\ ^\circ\text{C}^{-1}.$$

The mean of H_U and H_L can considered as the actual (corrected) meridional heat transport H of the experiment. Thus,

$$H \equiv H_U - (T_{\text{water}} - T_{\text{lab}}) \times 1.5\ \text{W}^\circ\ \text{C}^{-1}. \quad \text{(A1)}$$

Here T_{lab} is the temperature of the laboratory, which was set to 20 (± 1)°C using a laboratory-wide temperature and humidity controller. Thus, T_{lab} can be considered the same as the temperature of the cold water bath T_B = 20°C. It was assumed that the water in the tank was homogeneous and the temperature was T_{water}.

If the thermal boundary layer of the experiment is excluded, the water temperature shows very little spatial changes, so T_{water} could be considered as the highest temperature measured throughout a run. The typical uncertainty in H due to H_U and H_L is about 20%. Hereafter, H or meridional heat flux means the corrected value using Eq. (A1) and H_N or nominal heat flux means $H_{\text{heating pad}}$.

Tables

Table 1. The power dependence of δ_T on f using linear least squares fit for fixed H_N.

	H_N (W)				
	20	50	100	200	Mean
Power dependence	0.20	0.29	0.27	0.50	0.32
Residual	0.04	0.04	0.03	0.05	0.04

Click on thumbnail for full-sized image.

APPENDIX B Parameters of the Experiments

0.25	20	15	3.6	3.2	0.52	2.7	13
0.63	20	14	3.8	3.5	0.55	1.1	32
1.25	20	14	4.2	4.5	0.61	0.54	62
0.25	50	40	6.4	2.2	0.93	2.7	11
0.32	50	40	6.4	2.7	0.93	2.1	14
0.45	50	40	6.6	2.7	0.96	1.5	19
0.63	50	40	7.0	3.3	1.0	1.1	25
1.00	50	39	7.3	3.4	1.1	0.68	39
1.25	50	39	7.5	3.5	1.1	0.54	49
0.25	100	86	9.7	1.7	1.4	2.7	9
0.32	100	84	10.8	2.0	1.6	2.1	11
0.45	100	83	11.5	2.3	1.7	1.5	15
0.63	100	82	11.8	2.4	1.7	1.1	20
1.00	100	81	12.4	2.6	1.8	0.68	32
1.25	100	81	13.0	2.8	1.9	0.54	40
0.25	200	177	15.5	1.3	2.3	2.7	7
0.32	200	175	16.6	1.1	2.4	2.1	9
0.54	200	174	17.4	1.6	2.5	1.3	15
0.63	200	173	18.2	1.6	2.7	1.1	17
1.00	200	171	18.9	2.5	2.8	0.68	27
1.25	200	170	19.8	2.5	2.9	0.54	33
0.25	300	271	19.5	—	2.8	2.7	7
0.63	300	268	21.6	—	3.1	1.1	16
1.25	300	266	22.7	—	3.3	0.54	32

Click on thumbnail for full-sized image.

Figures

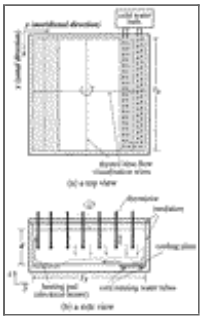

Click on thumbnail for full-sized image.

Fig. 1. The design of the experiment: (a) a top view and (b) a side view along a meridional section. The tank is 100 cm × 100 cm × 20 cm. The thermal forcing was applied using an electrical heater and a cooling plate along the bottom of the tank. The configuration is equivalent to an upside-down *f*-plane ocean with constant heat flux at the bottom.

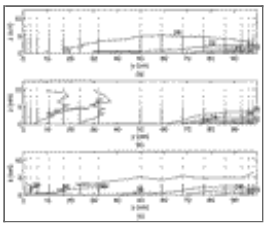

Click on thumbnail for full-sized image.

Fig. 2. Meridional temperature sections at $x = 50$ cm with (a) $f = 0.63\ \mathrm{s}^{-1}$ and $H_N = 50$ W, (b) $f = 1\ \mathrm{s}^{-1}$ and $H_N = 50$ W, and (c) $f = 1\ \mathrm{s}^{-1}$ and $H_N = 200$ W. The meridional wall to the left when looking toward the cold end is at $x = 0$ cm and is equivalent to the eastern boundary of the oceans. The dots indicate the location of temperature measurements. The heating plate is 0 cm $\leqslant y \leqslant$ 20.3 cm and the cooling plate is 79.7 cm $\leqslant y \leqslant$ 100 cm.

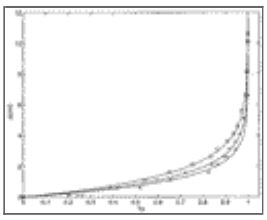

Click on thumbnail for full-sized image.

Fig. 3. Normalized temperature profiles at $(x, y) = (49.5\ \mathrm{cm}, 96\ \mathrm{cm})$ (○: $f = 1.25\ \mathrm{s}^{-1}$, $H_N = 50$ W; +: $f = 0.45\ \mathrm{s}^{-1}$, $H_N = 50$ W; ×: $f = 1.25\ \mathrm{s}^{-1}$, $H_N = 200$ W). Solid curves are the least square fits of profiles to exponential functions.

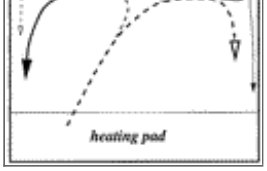

Click on thumbnail for full-sized image.

Fig. 4. A schematic diagram of flow pattern. A solid curve represents cold current and a dotted curve represents warm current. If a solid curve and a dotted curve are stacked, the cold flow is near the bottom and warm flow is above the cold flow.

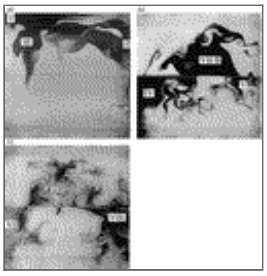

Click on thumbnail for full-sized image.

Fig. 5. Flow pattern viewed from above when $f = 1\ s^{-1}$ and $H_N = 50$ W. The cold end wall is at the top and the hot wall is at the bottom. In (a) $y = 90$ cm (over the cooling plate), $z = 1$ cm, and $t = 30$ min; (b) $y = 50$ cm (along the center zonal section), $z = 1$ cm, and $t = 30$ min; (c) $y = 50$ cm, $z = 7$ cm, and $t = 30$ min.

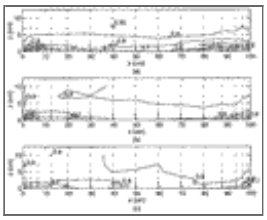

Click on thumbnail for full-sized image.

Fig. 6. Zonal temperature sections when $f = 1\ s^{-1}$ and $H_N = 50$ W (a) $y = 70$ cm, (b) $y = 50$ cm, and (c) $y = 30$ cm.

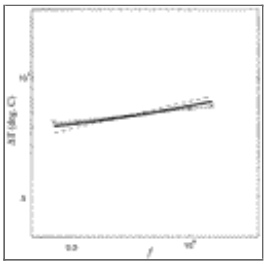

Click on thumbnail for full-sized image.

Fig. 7. Plot of ΔT vs f when $H_N = 50$ W. The experimental results are shown using "×." The thin solid line (slope = 0.13) is the least squares fit to the data. The dashed line (slope = ¼) is for the geostrophic scaling law. The thick solid line (mean slope = 0.17) is for the corrected scaling law discussed in section 4d. A proportionality constant of about 3 was applied to fit the scaling laws to the data.

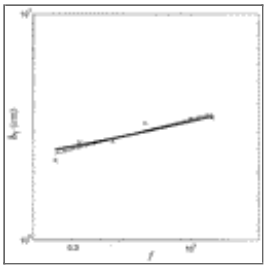

Click on thumbnail for full-sized image.

Fig. 8. Plot of δ_T vs f when $H_N = 50$ W. The experimental results are shown using "×." The thin solid line (slope = 0.29) is the least squares fit to the data. The dashed line (slope = ¼) is for the geostrophic scaling law. The thick solid line is for the corrected

scaling law discussed in section 4d.

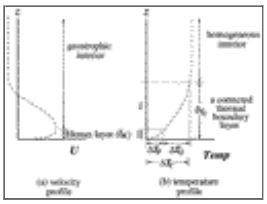

Click on thumbnail for full-sized image.

Fig. 9. Schematic profiles of (a) velocity and (b) temperature.

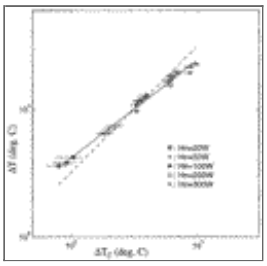

Click on thumbnail for full-sized image.

Fig. 10. Comparison of $\Delta T_C(f, H)$ from the corrected scaling law and the experiment. The dashed line is from the scaling law with a proportionality constant 2.7. The solid line is the least squares fit of the experimental data.

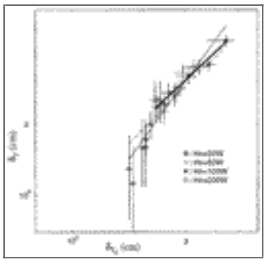

Click on thumbnail for full-sized image.

Fig. 11. Comparison of the corrected scaling law δ_{T_C} and the experimental results δ_T. The dashed line is from the geostrophic scaling law with a proportionality constant, 1.0. The thin solid line is the least squares fit of all the data and the thick solid line is the least squares fit of $\delta_{T_{\text{exp}}} > 2$ cm.

* Woods Hole Oceanographic Institution Contribution Number 9458.

Corresponding author address: Dr. Young-Gyu Park, Center for Ocean-Land-Atmosphere Studies, 4041 Powder Mill Road, Suite 302, Calverton, MD 20705-3106.

E-mail: ypark@cola.iges.org

top